I R I S A
INSTITUT DE RECHERCHE EN INFORMATIQUE ET SYSTÈMES ALÉATOIRES

PUBLICATION
INTERNE
N° 1858

KINEMATIC VISUAL SERVO CONTROL OF A QUADROTOR AERIAL VEHICLE

ODILE BOURQUARDEZ, ROBERT MAHONY,
NICOLAS GUENARD, FRANÇOIS CHAUMETTE,
TAREK HAMEL, LAURENT ECK

ISSN 1166-8687

IRISA
CAMPUS UNIVERSITAIRE DE BEAULIEU - 35042 RENNES CEDEX - FRANCE

IRISA

INSTITUT DE RECHERCHE EN INFORMATIQUE ET SYSTÈMES ALÉATOIRES
Campus de Beaulieu – 35042 Rennes Cedex – France
Tél. : (33) 02 99 84 71 00 – Fax : (33) 02 99 84 71 71
http://www.irisa.fr

Kinematic Visual Servo Control of a Quadrotor aerial vehicle

Odile Bourquardez[♣] , Robert Mahony[♮] , Nicolas Guenard[△] ,

François Chaumette[♠] , Tarek Hamel[*] , Laurent Eck[◇]

Systèmes cognitifs
Projet Lagadic

Publication interne n ° 1858 — Juillet 2007 — 36 pages

Abstract: Visual systems are key sensors for control of small scale unmanned aerial vehicles. In this paper we investigate a range of image based visual servo control algorithms for positioning of flying vehicles capable of hover. The image based outer control loop for translation kinematics is coupled to a high-gain inner control loop that regulates translational velocities and full attitude dynamics. Zero and first order image moments are used as visual features for the control design. Perspective projection moments with suitable scaling along with a classical image based visual servo control design lead to satisfactory transients and asymptotic stability of the closed-loop system when the image plane remains parallel to the target. However, the system response may lack robustness for aggressive manoeuvres. In order to overcome this problem, several control schemes, based on spherical image moments, are designed and their performance is analysed. All designed control laws have been tested on a kinematic robotic manipulator to demonstrate the relative strengths and weaknesses of the different image based visual servo control designs. The three most promising control algorithms have been successfully implemented on an autonomous aerial vehicle showing excellent performances in all three cases.

Key-words: visual servoing, aerial robotic vehicle

(Résumé : tsvp)

♣ Odile.Bourquardez@irisa.fr
♮ Department of Engineering, Australian National University, Canberra, ACT 0200, Australia Robert.Mahony@anu.edu.au
△ CEA/List, BP 6, 92265 Fontenay-aux-Roses cedex, France Nicolas.Guenard@cea.fr
♠ Francois.Chaumette@irisa.fr
* I3S, UNSA - CNRS, BP 121, 06903 Sophia Antipolis, France thamel@i3s.unice.fr
◇ CEA/List, BP 6, 92265 Fontenay-aux-Roses cedex, France Laurent.Eck@cea.fr

Centre National de la Recherche Scientifique (UMR 6074) Université de Rennes 1 – Insa de Rennes
Institut National de Recherche en Informatique et en Automatique – unité de recherche de Rennes

Asservissement visuel cinématique pour un robot volant à quatre rotors

Résumé : Les capteurs de vision sont des systèmes prometteurs pour la commande d'engins volants autonomes. Dans ce rapport, nous nous intéressons plus particulièrement à commander la position des robots volants capables d'évoluer en vol stationnaire. Nous proposons pour cela une série de schémas de commande d'asservissement visuel. Le schéma de commande est conçu sous la forme de deux boucles imbriquées : une boucle externe d'asservissement visuel, qui s'appuie sur une boucle interne à grand gain. Cette dernière régule les vitesses de translation fournies par l'asservissement visuel, et commande les mouvements de rotation induits par la dynamique de l'engin. Les informations visuelles que nous considérons sont des moments d'ordre zéro et un. Une première approche consiste à utiliser les moments de l'image perspective, avec un changement d'échelle bien choisi. Une loi de commande classique d'asservissement visuel donne des résultats satisfaisants en terme de comportement transitoire et de stabilité asymptotique du système bouclé, quand le plan image est parallèle à la cible considérée. Cependant, cette approche n'est pas adaptée à la dynamique de tous les engins, et peut donc manquer de robustesse lors de manœuvres agressives. L'utilisation du centre de gravité de l'image sphérique permet de réaliser des lois de commande tenant compte de la dynamique des robots volants considérés. Dans ce rapport, nous développons et analysons plusieurs schémas de commande d'asservissement visuel reposant sur cette information visuelle. Toutes les lois de commande proposées ont été testées sur un robot de type bras manipulateur, afin de mettre en évidence leurs atouts et leurs faiblesses. Les trois schémas de commande les plus intéressants ont également été implémentés sur un robot volant à quatre rotors. Les résultats obtenus sont très satisfaisants.

Mots clés : asservissement visuel, robot volant

1 Introduction

Visual servo algorithms have been extensively developed in the robotics field over the last ten years [7, 21, 15]. Visual servo systems may be divided into two main classes [20]: *Position-based visual servo* (PBVS) involves reconstruction of the target pose with respect to the robot and results in a Cartesian motion planning problem. This approach requires an accurate 3D model of the target, displays high sensitivity to image noise, poor robustness of pose estimation and the tendency for image features to leave the camera field of view during the task [4]. *Image-based visual servo* (IBVS) treats the problem as one of controlling features in the image plane, such that moving features to a goal configuration implicitly accomplishes the task [7, 22]. This approach does not require a 3D model of the target, is robust to camera calibration errors and can generally be implemented to ensure image features do not leave the camera field of view during the task [4]. However, for an IBVS control system, good closed-loop behaviour in image space does not necessarily imply good transient behaviour in task space [4, 17]. Image moments are a useful and robust image feature for IBVS control [5]. A desirable property of particular combination of image moments is their invariance properties [24]. In particular, the norm of certain spherical image moments are invariant to rotational motion, a property that was used to extend image based visual servo to the control of under-actuated dynamic systems such as helicopters [13]. A further desirable property of spherical image moments is that the translational part of the interaction matrix is a positive definite matrix; a property that can be exploited to design of globally stabilising image based visual servo control laws.

In this paper we provide an analysis of image based visual servo (IBVS) control for a class of image features based on first order spherical moments. Using centroid information is an old technique in visual servo control [8, 1, 23, 16, 25, 5]. The calculation of image moments is highly robust to pixel noise, can be easily implemented in real-time, and does not require matching observed features with a target configuration that would be required for classical image based visual servo control based on more traditional image features such as points and lines [15]. The goal of this paper is to investigate a range of control designs based on the proposed image feature and use this to understand the important properties of visual servo control algorithms for unmanned aerial vehicles. In particular, we are interested in the properties of global asymptotic stability (GAS) and performance of the closed-loop system. Global asymptotic stability refers to the abstract property of a controller to stabilise the pose of the camera from any initial condition. Image based visual servo systems that are not GAS have fundamental instability built into their formulation. There are a number of examples of such systems in the literature [4, 19]. The question of performance is also a key issue in the design of image based visual servo controllers. Since the dynamics of the system are controlled in image space, there is no guarantee that the closed-loop response in task space is acceptable. The most common problem that occurs is one of relative sensitivity where not all coordinates of the pose in task space converge at equal rates, leading to poor performance of the closed-loop system. To investigate these properties we propose a range of GAS and locally exponentially stable controllers defined in the image space. The performances of the kinematic closed-loop system are experimentally verified on a 6 degrees

of freedom robotic manipulator. The most promising control laws were implemented as a velocity control demand on an aerial robot equipped with a separate high-gain regulator for the dynamic response. The closed-loop response of the physical system shows excellent robustness and performance. The present paper is an extension of earlier work [3] of the authors.

The paper is organized as follows. Section 2 develops a classical IBVS control scheme using perspective image moments. Section 3 introduces the definition and properties of first order spherical image moments and presents a range of control laws for the translational motion of the camera using this visual feature. Stability and performance of the closed-loop system are studied for each control law, and experimental results using a 6 degrees of freedom holonomic robot are reported. Section 4 provides an analysis and a comparison of the control laws proposed. The three most promising control algorithms have been implemented on a quadrotor aerial vehicle, and the experimental results are presented and their relative performance is analysed in Section 5.

2 Perspective projection

In this section, an image based visual servo control for regulation of the translation kinematics of a vehicle is presented. The image features used are perspective projection image moments [24] that are chosen to obtain a quasi-linear and decoupled image kinematics.

Let $\mathcal{A}$ denote the inertial or task space reference frame and let $\mathcal{C}$ denote the camera or body-fixed reference frame. Let (u, v) denote the 2D pixel locations of an observed point. Assume that a camera calibration matrix $\mathbf{K}$ is available. Let $\bar{\mathbf{p}} = (x, y, 1)$ denote a point on the image plane corresponding to pixel (u, v). One has

$$\begin{pmatrix} u \\ v \\ 1 \end{pmatrix} = \mathbf{K}\bar{\mathbf{p}}. \tag{1}$$

Let $\mathcal{S}_p$ denote the observed image of a target on the camera image plane S_p^2. The 2D moments m_{pq} of order $p + q$ are

$$m_{pq} = \iint_{\bar{\mathbf{p}} \in \mathcal{S}_p} x^p y^q dx dy.$$

The area a and the centroid coordinates x_g, y_g of the object in the image are defined using the zero and first order moments: $a = m_{00}$, $x_g = \frac{m_{10}}{a}$ and $y_g = \frac{m_{01}}{a}$.

In order to obtain a quasi linear and decoupled link between the image space and the task space, the visual feature vector $\mathbf{s} = (x_n, y_n, a_n)$ is defined such that [24]

$$a_n = Z^* \sqrt{\frac{a^*}{a}}, \quad x_n = a_n x_g, \quad y_n = a_n y_g$$

where a^* is the desired area and Z^* the desired depth between the camera and the target. The time derivative of $\mathbf{s}$ and the relative motion between the camera and the object can be related by the classical equation

$$\dot{\mathbf{s}} = \mathbf{L}_{\boldsymbol{\upsilon}} \boldsymbol{\upsilon} + \mathbf{L}_{\boldsymbol{\omega}} \boldsymbol{\omega} \tag{2}$$

where $\boldsymbol{\upsilon}$ and $\boldsymbol{\omega}$ are respectively the linear and angular velocity of the camera both expressed in the camera frame, and where $\mathbf{L}_{\boldsymbol{\upsilon}}$ and $\mathbf{L}_{\boldsymbol{\omega}}$ are respectively the parts of the interaction matrix related to the translational and the rotational motions. The desired image feature is denoted by $\mathbf{s}^* \in \mathcal{C}$, and the visual error is defined by $\mathbf{e} = \mathbf{s} - \mathbf{s}^*$.

Classical image based visual servo control design aims to impose linear exponential stability on the image error kinematics [7, 20, 24] to ensure an exponential decoupled decrease for $\mathbf{e}$ ($\dot{\mathbf{e}} = -\lambda \mathbf{e}$). Using $\mathbf{e}$ to control the translational degrees of freedom, the classical IBVS control input is:

$$\boldsymbol{\upsilon} = -(\mathbf{L}_{\boldsymbol{\upsilon}})^{-1}(\lambda \mathbf{e} + \mathbf{L}_{\boldsymbol{\omega}} \boldsymbol{\omega}), \quad \lambda > 0. \tag{3}$$

Generally, the interaction terms $\mathbf{L}_{\boldsymbol{\upsilon}}$ and $\mathbf{L}_{\boldsymbol{\omega}}$ depend non-linearly on the state of the system and cannot be reconstructed exactly from the observed visual data. The visual

feature $\mathbf{s} = (x_n, y_n, a_n)$ is of particular interest since $\mathbf{L}_{\boldsymbol{v}} = -\mathbf{I}_3$ in the case where the camera image plane is parallel to the target plane [24]. In the application considered in Section 5, the camera is mounted to point directly downward in the quadrotor and the image and target plane are never more than a couple of degrees offset. As a consequence, the approximation $\mathbf{L}_{\boldsymbol{v}} \approx -\mathbf{I}_3$ is valid. The control law is thus simplified to

$$\boldsymbol{v} = \lambda \mathbf{e} + \mathbf{L}_{\boldsymbol{\omega}} \boldsymbol{\omega}, \quad \lambda > 0. \tag{4}$$

Since the link between image space and task space is almost linear and decoupled ($\mathbf{L}_{\boldsymbol{v}} \approx -\mathbf{I}_3$), this control scheme is known to lead to satisfactory closed-loop behaviour for holonomic robot [24]. It is in fact equivalent to a position-based visual servo, but without any pose estimation required.

The motion of the quadrotor is smooth and slow and the value of $\mathbf{L}_{\boldsymbol{\omega}} \boldsymbol{\omega}$ is small compared with the error $\lambda \mathbf{e}$ in (4). Thus, a reasonable approximation of (4) for the purposes of this paper is

$$\boldsymbol{v} = \lambda \mathbf{e}, \quad \lambda > 0. \tag{5}$$

Equation (5) does not require the estimation of any 3D parameters and can be implemented based only on the observed image features $\mathbf{s}$. This control was implemented on the experimental platform and the results are discussed in Section 4. The limitation of this approach, however, lies in its dependence on the particular geometry of the application considered and the requirement to consider only smooth slow trajectories of the vehicle. If the vehicle undertakes aggressive manoeuvres, or the parallel target plane assumption is invalidated for a particular application, the approximation $\mathbf{L}_{\boldsymbol{v}} \approx -\mathbf{I}_3$ will fail and more importantly the approximation $\mathbf{L}_{\boldsymbol{\omega}} \boldsymbol{\omega} \approx \mathbf{0}$ may also fail. This second issue introduces a significant dynamic disturbance in the system response that cannot be cancelled directly without the risk of introducing zero dynamic effects into the closed-loop response similar to those studied in recent works [9, 14, 18]. The potential limitations of the classical IBVS control design based on perspective projection features motivate us to consider a class of spherical projection features and non-linear control design techniques.

3 Spherical projection

3.1 Modelling

In this section we use an un-normalised first order spherical image moment along with an inertial goal vector to generate an image error.

A spherical camera geometry with unity radius is used. Let $\mathbf{p}$ denote a point on the spherical image surface corresponding to perspective point $\bar{\mathbf{p}}$ (fig.1). One has

$$\mathbf{p} = \frac{\bar{\mathbf{p}}}{|\bar{\mathbf{p}}|}. \tag{6}$$

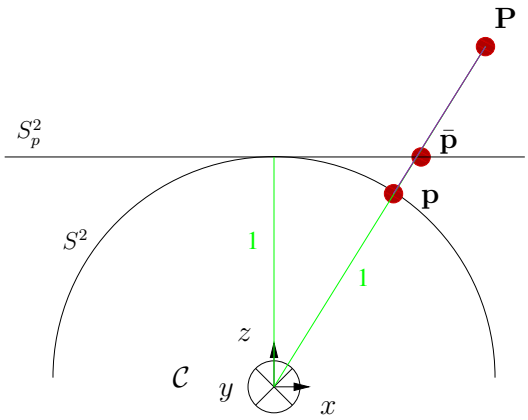

Figure 1: Perspective $\bar{\mathbf{p}}$ and spherical $\mathbf{p}$ projections of a 3D point $\mathbf{P}$.

Let $\mathcal{S}$ denote the observed image of a target on the spherical camera image plane S^2. The first order un-normalised moment (or centroid) is

$$\mathbf{q} := \int_{\mathbf{p}\in\mathcal{S}} \mathbf{p}d\mathbf{p}.$$

In practice, a common approach is to use point targets rather than continuous surfaces. Consider a point target consisting of n points $\{\mathbf{P}_i\} \in \mathcal{C}$ corresponding to image points $\{\mathbf{p}_i\}$. The centroid of a target is defined to be

$$\mathbf{q} := \sum_{i=1}^{n} \mathbf{p}_i \in \Re^3. \tag{7}$$

In both cases the centroid $\mathbf{q}$ is a three-dimensional vector. Thanks to the spherical camera geometry, the third entry of the centroid is non-linearly related to depth of the camera from the observed target constellation.

For a point target comprising a finite number of image points the kinematics of the image centroid are easily verified to be [13]

$$\dot{\mathbf{q}} = -\boldsymbol{\omega} \times \mathbf{q} - \mathbf{Q}\boldsymbol{v}, \tag{8}$$

where

$$\mathbf{Q} = \sum_{i=1}^{i=n} \frac{\boldsymbol{\pi}_{\mathbf{p}_i}}{|\mathbf{P}_i|} \tag{9}$$

and $\boldsymbol{\pi}_{\mathbf{p}} = (\mathbf{I}_3 - \mathbf{p}\mathbf{p}^\top)$.

As long as there are at least two points $\mathbf{p}_i$ in image space the matrix $\mathbf{Q}$ is positive definite [13].

Let $\mathbf{b} \in \mathcal{A}$ denote the fixed desired set point for the visual feature $\mathbf{q}$. The feature $\mathbf{q}$ is measured relative to the camera frame, and it is necessary to map the desired set point into the camera frame before an image based error can be defined.

Let $\mathbf{q}^* := \mathbf{R}^\top \mathbf{b} \in \mathcal{C}$, where rotation matrix $\mathbf{R}$ between the camera frame and the inertial frame is assumed to be known, a common assumption when dealing with the control of underactuated systems such as helicopters [13].

The image based error considered is

$$\boldsymbol{\delta} := \mathbf{q} - \mathbf{q}^*. \tag{10}$$

The reason for choosing the image error in this manner is that it ensures the passivity-like structure of the error kinematics [13].

Since $\mathbf{q}^* \in \mathcal{C}$, it inherits dynamics from the motion of the camera: $\dot{\mathbf{q}}^* = -\boldsymbol{\omega} \times \mathbf{q}^*$. Thus, the image error kinematics are

$$\dot{\boldsymbol{\delta}} = \boldsymbol{\delta} \times \boldsymbol{\omega} - \mathbf{Q}\boldsymbol{v}. \tag{11}$$

This can be written as an interaction matrix

$$\dot{\boldsymbol{\delta}} = \begin{bmatrix} -\mathbf{Q} & \boldsymbol{\delta}_\times \end{bmatrix} \begin{bmatrix} \boldsymbol{v} \\ \boldsymbol{\omega} \end{bmatrix}$$

where $\boldsymbol{\delta}_\times$ is the skew symmetric matrix such that $\boldsymbol{\delta}_\times \mathbf{w} = \boldsymbol{\delta} \times \mathbf{w}$ for any vector $\mathbf{w}$.

Taking the time derivative of $|\boldsymbol{\delta}|$ and substituting for (11) yields:

$$|\dot{\boldsymbol{\delta}}| = \frac{1}{|\boldsymbol{\delta}|}\boldsymbol{\delta}^\top \dot{\boldsymbol{\delta}} = \frac{1}{|\boldsymbol{\delta}|}(\boldsymbol{\delta}^\top \boldsymbol{\delta}_\times \boldsymbol{\omega} - \boldsymbol{\delta}^\top \mathbf{Q}\boldsymbol{v}).$$

A well-known property of skew symmetric matrix gives $\boldsymbol{\delta}^\top \boldsymbol{\delta}_\times = \mathbf{0}$. Thus, one obtains

$$|\dot{\boldsymbol{\delta}}| = -\frac{\boldsymbol{\delta}^\top \mathbf{Q}\boldsymbol{v}}{|\boldsymbol{\delta}|}. \tag{12}$$

It follows that $|\boldsymbol{\delta}|$ is a function of position only.

Another important property is that the image error expressed in the inertial frame $\boldsymbol{\delta}_0 := \mathbf{R}\boldsymbol{\delta}$ is a function of position only. Indeed, since $\dot{\mathbf{R}} = \mathbf{R}\boldsymbol{\omega}_\times$, and recalling (11) one obtains

$$\dot{\boldsymbol{\delta}}_0 = \mathbf{R}(\boldsymbol{\delta}_\times \boldsymbol{\omega} - \mathbf{Q}\boldsymbol{v}) + \mathbf{R}\boldsymbol{\omega}_\times \boldsymbol{\delta} = -\mathbf{R}\mathbf{Q}\boldsymbol{v}. \tag{13}$$

As a consequence, $\boldsymbol{\delta}_0$ is independent of the camera rotational motion.

3.2 Experimental conditions

The control designs discussed below have been first implemented on a holonomic 6 degrees of freedom robot to verify closed-loop kinematic performance. These results are presented along with the derivations. The target used was a four white marks on the vertices of a planar rectangle (the target size is 14×10 cm). In all the reported experiments, the initial and desired positions in 3D were the same. The desired vector $\mathbf{q}^*$ was chosen such that the camera set point was located at 0.5 m above the target. Figure 2 shows the initial and goal appearance of the target. The end-effector of the robot was moved in translation according to the control law presented below. A classical IBVS control law was used to control the rotational degrees of freedom. The target centroid and its orientation in the perspective image plane was used to control these three degrees of freedom [5].

The asymptotic value $\mathbf{Q}^*$ of the matrix $\mathbf{Q}$ (cf. Eq. (9)) at the limit point was $\mathbf{Q}^* \simeq \mathrm{diag}(7.73, 7.81, 0.226)$.

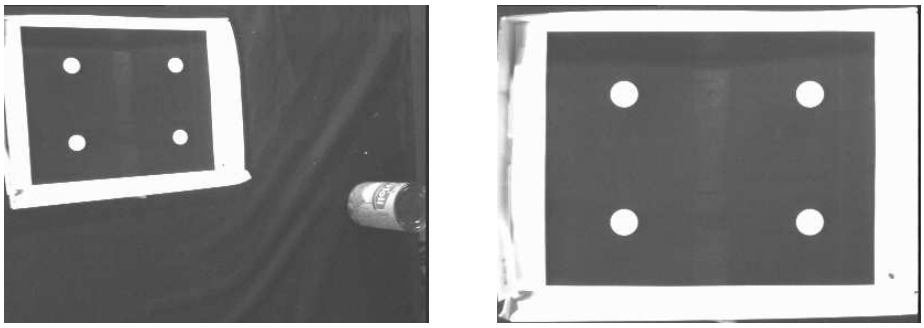

(a) (b)

Figure 2: (a) Initial image, (b) Desired image.

3.3 Proportional control

This subsection considers pure proportional feedback of the un-normalized centroid [13].

Define a storage function $\mathcal{L}$ by

$$\mathcal{L} = \frac{1}{2}|\boldsymbol{\delta}|^2. \tag{14}$$

From (12) we obtain immediately

$$\dot{\mathcal{L}} = -\boldsymbol{\delta}^\top \mathbf{Q}\boldsymbol{v}. \tag{15}$$

The matrix $\mathbf{Q}$ is not exactly known, however, as mentioned earlier, it is known to be positive definite. Thus, a simple choice

$$\boldsymbol{v} = k_{\boldsymbol{\delta}}\boldsymbol{\delta}, \quad k_{\boldsymbol{\delta}} > 0 \tag{16}$$

is sufficient to stabilise $\mathcal{L}$. Indeed, by substituting the control input $\boldsymbol{v}$ by its expression in (15), one obtains

$$\dot{\mathcal{L}} = -k_{\boldsymbol{\delta}} \boldsymbol{\delta}^\top \mathbf{Q} \boldsymbol{\delta}. \tag{17}$$

Since $\mathbf{Q}$ is a positive definite matrix, classical Lyapunov theory guarantees that $\boldsymbol{\delta}$ converges exponentially to zero.

Note, however, that the matrix $\mathbf{Q}$ is not well-conditioned; in the general case $\lambda_{\min}(\mathbf{Q}) << \lambda_{\max}(\mathbf{Q})$. This means that convergence rates of the components of $\boldsymbol{\delta}$ are not equal and the component which is affected by the eigenvalue $\lambda_{\min}(\mathbf{Q})$ is more sensitive to perturbations. By computing the matrix $\mathbf{Q}$ at the desired position ($\mathbf{Q}^*$), it follows that $\lambda_{\min}$ is the third eigenvalue of matrix $\mathbf{Q}$. The third component of $\mathbf{q}$ (or $\boldsymbol{\delta}$) is thus sensitive to perturbations.

The experimental results obtained using control scheme (16) are reported on Fig. 3. We have chosen to depict $\boldsymbol{\delta}_0 = \mathbf{R}\boldsymbol{\delta}$ since, as shown in (13), it is independent of the camera rotational motion, and is thus not perturbed by the additional control law we have used to control the rotational motion. The camera position $\boldsymbol{\xi}_0$ measured thanks to the robot odometry, and expressed in the inertial frame, is also depicted.

We can see on Fig. 3.a that the convergence of $\boldsymbol{\delta}_{0z}$ is very slow compared to the convergence of the other components $\boldsymbol{\delta}_{0x}$ and $\boldsymbol{\delta}_{0y}$. Similarly, in task space, we must wait for a large number of iterations so that the depth component converges to the desired value, whereas the lateral and longitudinal components converge in few iterations (Fig. 3.b).

Although this control law ensures global asymptotic stability, the task space and image space behaviour are not acceptable.

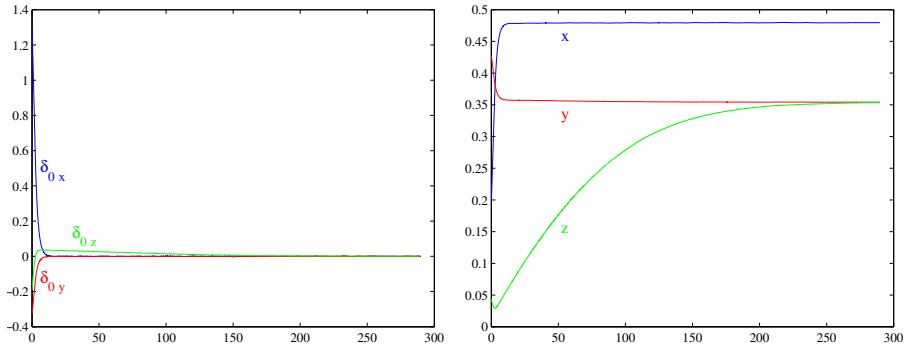

(a) (b)

Figure 3: Proportional control $\boldsymbol{v} = k\boldsymbol{\delta}$: time evolution of the image feature $\boldsymbol{\delta}_0 = \mathbf{R}\boldsymbol{\delta}$ (a), and of the pose $\boldsymbol{\xi}_0$ (b).

3.4 Linearization at the set point

The first idea for compensating the poor sensitivity in the previous control design is to use the inverse interaction matrix, analogous to standard practice in classical IBVS [15]. Indeed the choice $\boldsymbol{\upsilon} = k_{\mathbf{Q}}\mathbf{Q}^{-1}\boldsymbol{\delta}$, $k_{\mathbf{Q}} > 0$ yields $\dot{\mathcal{L}} = -k_{\mathbf{Q}}\boldsymbol{\delta}^{\top}\mathbf{Q}\mathbf{Q}^{-1}\boldsymbol{\delta} = -k_{\mathbf{Q}}\boldsymbol{\delta}^{\top}\boldsymbol{\delta}$. This choice guarantees global asymptotic stability and ensures equal convergence rates. However the matrix $\mathbf{Q}^{-1}$ is not exactly known, since it depends on the 3D depths $|\mathbf{P}_i|$, and an approximate cancellation is used in practice.

The most common approximation is to use the *desired* interaction matrix $\mathbf{Q}^*$ instead of the *current* interaction matrix $\mathbf{Q}$ [4]:

$$\boldsymbol{\upsilon} = k_*\mathbf{Q}^{*-1}\boldsymbol{\delta}, \quad k_* > 0. \tag{18}$$

The Lyapunov function derivative becomes

$$\dot{\mathcal{L}} = -k_{\mathbf{Q}}\boldsymbol{\delta}^{\top}\mathbf{Q}\mathbf{Q}^{*-1}\boldsymbol{\delta}$$

and remains negative as long as $\mathbf{Q}\mathbf{Q}^{*-1}$ is positive definite.

As can be seen on Fig. 4, this control law enables equal convergence rates of the visual error components (Fig. 4.a), and equal convergence rates in task space (Fig. 4.b). However, in practice, this control scheme is adequate only in the neighborhood of the desired position. Indeed we can see on Fig. 4.b that the transient behaviour of the depth Z in task space is not acceptable.

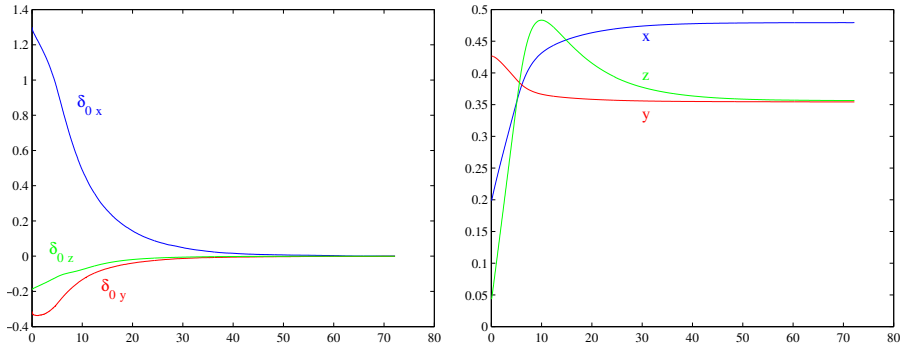

(a) (b)

Figure 4: Asymptotic linearising control $\boldsymbol{\upsilon} = k_*\mathbf{Q}^{*-1}\boldsymbol{\delta}$: time evolution of the image feature $\boldsymbol{\delta}_0 = \mathbf{R}\boldsymbol{\delta}$ (a), and of the pose $\boldsymbol{\xi}_0$ (b).

3.5 Partitioned control

Since difficulties observed in the two control designs presented in Sections 3.3 and 3.4 result from sensitivity in the z-axis, a possible solution is to use a partitioned approach by singling out the problematic component for a special treatment [6].

We separate the visual error term into two criteria with different sensitivity. Two new error terms are introduced in order to compensate the poor sensitivity of $\mathbf{q}$:

$$\boldsymbol{\delta}_{11} = \mathrm{sk}(\mathbf{q}_0^*)\mathbf{q}, \quad \delta_{12} = \mathbf{q}_0^{*\top}\boldsymbol{\delta}, \quad \text{with } \mathbf{q}_0^* = \frac{\mathbf{q}^*}{|\mathbf{q}^*|}.$$

Note that due to the properties of the skew symmetric matrix $\mathrm{sk}(\mathbf{q}_0^*)$, $\boldsymbol{\delta}_{11}$ and $\mathbf{q}_0^*\delta_{12}$ are orthogonal. δ_{12} is the projection of the error $\boldsymbol{\delta}$ along the $\mathbf{q}^*$ direction.

Deriving $\boldsymbol{\delta}_{11}$ and δ_{12}, it follows that

$$\dot{\boldsymbol{\delta}}_{11} = -\mathrm{sk}(\boldsymbol{\omega})\boldsymbol{\delta}_{11} - \mathrm{sk}(\mathbf{q}_0^*)\mathbf{Q}\boldsymbol{\upsilon}, \tag{19}$$

$$\dot{\delta}_{12} = -\mathbf{q}_0^{*\top}\mathbf{Q}\boldsymbol{\upsilon}. \tag{20}$$

Let us define as Lyapunov function $\mathcal{L}$ such that

$$\mathcal{L} = \frac{1}{2}(|\boldsymbol{\delta}_{11}|^2 + \lambda^2\delta_{12}^2) \tag{21}$$

where λ is a constant chosen as shown below. It is straightforward to verify that $\mathcal{L} = \frac{1}{2}|\boldsymbol{\delta}_{\mathbf{A}}|^2$, with

$$\boldsymbol{\delta}_{\mathbf{A}} = \boldsymbol{\delta}_{11} + \lambda\mathbf{q}_0^*\delta_{12}. \tag{22}$$

Deriving (21), recalling (19), (20), and substituting for (22), one obtains

$$\dot{\mathcal{L}} = -\boldsymbol{\delta}_{\mathbf{A}}^\top\mathbf{A}(\mathbf{q}_0^*)\mathbf{Q}\boldsymbol{\upsilon} \tag{23}$$

where $\mathbf{A}(\mathbf{q}_0^*) = \mathrm{sk}(\mathbf{q}_0^*) + \lambda\mathbf{q}_0^*\mathbf{q}_0^{*\top}$. We define the following control input

$$\boldsymbol{\upsilon} = k_{\mathbf{A}}\mathbf{A}(\mathbf{q}_0^*)^\top\boldsymbol{\delta}_{\mathbf{A}}, \quad k_{\mathbf{A}} > 0. \tag{24}$$

Recalling (23) and substituting the control input $\boldsymbol{\upsilon}$ by its expression yields

$$\dot{\mathcal{L}} = -k_{\mathbf{A}}\boldsymbol{\delta}_{\mathbf{A}}^\top\mathbf{A}(\mathbf{q}_0^*)\mathbf{Q}\mathbf{A}(\mathbf{q}_0^*)^\top\boldsymbol{\delta}_{\mathbf{A}}. \tag{25}$$

Since $\mathbf{Q}$ is a positive definite matrix and $\mathbf{A}(\mathbf{q}_0^*)$ a non singular matrix, $\mathbf{A}(\mathbf{q}_0^*)\mathbf{Q}\mathbf{A}(\mathbf{q}_0^*)^\top > \mathbf{0}$ and therefore $\boldsymbol{\delta}_{\mathbf{A}}$ converges exponentially to zero. Consequently, $\boldsymbol{\delta}_{11}$ and δ_{12} converge exponentially to zero (see (22)). Exponential convergence of the initial error $\boldsymbol{\delta}$ to zero is guaranteed.

Note that the best choice of the gain λ is characterized by the following constraint: $\mathbf{A}(\mathbf{q}_0^*)\mathbf{Q}^*\mathbf{A}(\mathbf{q}_0^*)^\top \cong \mathbf{I}_3$. where the symbol $\cong$ means "equality up to a multiplicative constant". This choice ensures asymptotically equivalent convergence rate for all the components of the error $\boldsymbol{\delta}_{\mathbf{A}}$. $\lambda = \sqrt{34}$ was used for the presented experimentations; it gave $\mathbf{A}(\mathbf{q}_0^*)\mathbf{Q}^*\mathbf{A}(\mathbf{q}_0^*)^\top \simeq \mathrm{diag}(7.8, 7.7, 7.7)$.

As can be seen on Fig. 5, the situation is quite similar to the previous one. The convergence rates are suitable in task space and in image space, but the transient behaviour of the depth Z is inappropriate. The system is theoretically stable, however in practice the control law can lead to very poor behaviour as soon as the distance between initial and desired position increases.

In fact we can see on Fig. 5.b that the transient behaviour of the Z position is worse than for the previous control design (Section 3.4): to achieve the task, the distance between the camera and the target should decrease, however, initially it increases. This behaviour is due to the fact that the partitioned control design uses $\mathbf{q}^*$ direction to separate the error $\boldsymbol{\delta}$ into two parts. This strategy is suitable asymptotically, when the optical axis direction is close to $\mathbf{q}^*$ direction (Fig. 6.a). But when the camera is too far from the desired position, $\boldsymbol{\delta}$ can project as can be seen on Fig. 6.b, that leads to $\delta_{12} < 0$ and then to an inappropriate velocity demand on the z-axis.

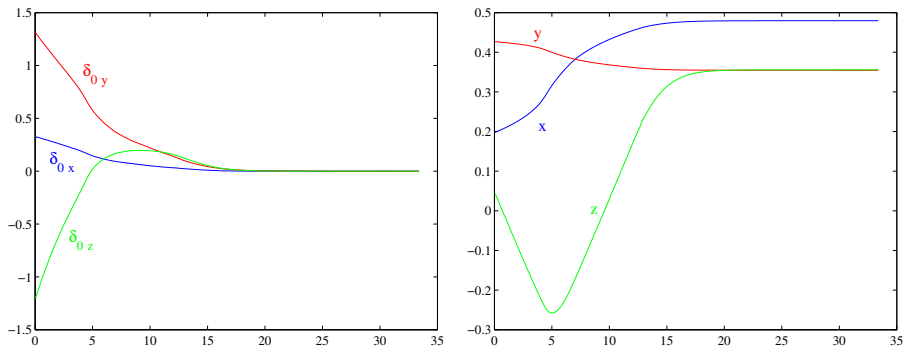

(a) (b)

Figure 5: Partitioned control $\boldsymbol{\upsilon} = k_{\mathbf{A}}\mathbf{A}(\mathbf{q}_0^*)^\top\boldsymbol{\delta}_{\mathbf{A}}$: time evolution of the image feature $\boldsymbol{\delta}_0 = \mathbf{R}\boldsymbol{\delta}_{\mathbf{A}}$ (a), and of the pose $\boldsymbol{\xi}_0$ (b).

3.6 Rescaled image feature

To improve the relationship between task space behaviour and image space behaviour, it is natural to try to determine an image feature that is as close to the 3D translation between the camera and the target as possible [24]. Such a choice leads to an interaction matrix close to the identity, leading to a linear and decoupled link between the image features and the translational degrees of freedom. Furthermore, satisfactory behaviour of the image features will automatically induce an acceptable behaviour in the task space.

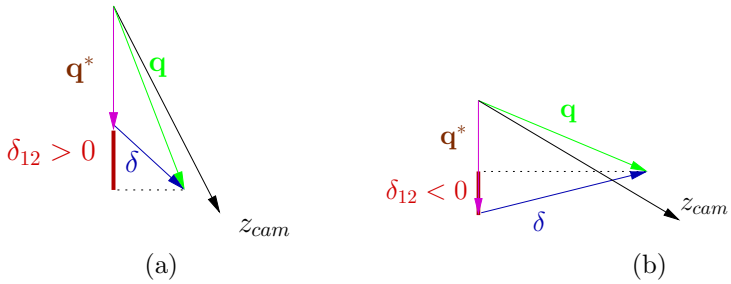

Figure 6: Near (a) and far (b) values of δ_{12}.

A rough approximation leads to the relationship between the actual depth Z from the geometric center of the target and the norm $|\mathbf{q}|$:

$$Z \simeq \frac{R|\mathbf{q}|}{\sqrt{n^2 - |\mathbf{q}|^2}}$$

where n is the number of points observed and R is the approximate radius of the target.

From Fig. 7, we can deduce that using the centroid $\mathbf{q}$ to servo depth as well as lateral position works well for manoeuvres where the camera is close to the target (where the depth sensitivity is approximately linear with $|\mathbf{q}|$). However, there is a significant loss of sensitivity as the camera moves away from the target.

From this relationship we propose to consider a new image feature

$$\mathbf{f} = F(|\mathbf{q}|)\mathbf{q}_0 \tag{26}$$

that incorporates the normalised first order moments $\mathbf{q}_0 = \frac{\mathbf{q}}{|\mathbf{q}|}$ along with the scaled "depth" parameter $F(|\mathbf{q}|)$ defined by

$$F(|\mathbf{q}|) := \frac{R|\mathbf{q}|}{\sqrt{n^2 - |\mathbf{q}|^2}}. \tag{27}$$

Note that $F(|\mathbf{q}|)$ depends on the radius of the target R. In fact this parameter acts only as a gain in the control design, and the properties of the control laws presented below are preserved as long as R is positive.

The error $\boldsymbol{\delta}_\mathbf{f}$ is defined as follows

$$\boldsymbol{\delta}_\mathbf{f} = \mathbf{f} - \mathbf{f}^* = F(|\mathbf{q}|)\mathbf{q}_0 - F(|\mathbf{q}^*|)\mathbf{q}_0^*. \tag{28}$$

Deriving (26) yields

$$\dot{\mathbf{f}} = \frac{\partial F(|\mathbf{q}|)}{\partial |\mathbf{q}|}\dot{|\mathbf{q}|}\mathbf{q}_0 + F(|\mathbf{q}|)\dot{\mathbf{q}}_0.$$

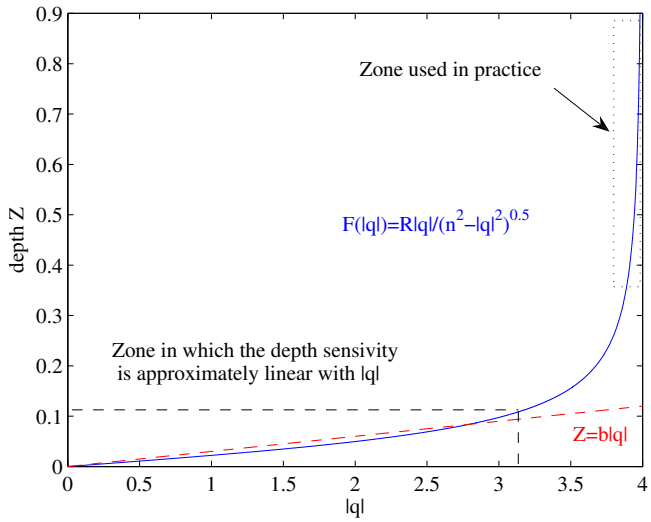

Figure 7: Plot of the relationship between the depth Z and the norm of the visual feature $|\mathbf{q}|$ (with $R = 0.086$, $n = 4$). Note that for $Z < 12$ cm then the sensitivity of the image feature to depth is approximately linear $Z \approx b|\mathbf{q}|$. For $Z > 12$ cm the sensitivity of depth to $|\mathbf{q}|$ is significantly reduced.

Using (8), we obtain after development:

$$\dot{\mathbf{f}} = -\boldsymbol{\omega} \times \mathbf{f} - \mathbf{M}\mathbf{Q}\boldsymbol{v}, \tag{29}$$

where

$$\mathbf{M}(\mathbf{q}) = \frac{\partial F(|\mathbf{q}|)}{\partial |\mathbf{q}|}\mathbf{q}_0\mathbf{q}_0^\top + \frac{F(|\mathbf{q}|)}{|\mathbf{q}|}(\mathbf{I}_3 - \mathbf{q}_0\mathbf{q}_0^\top). \tag{30}$$

Since $\dot{\mathbf{f}}^* = -\boldsymbol{\omega} \times \mathbf{f}^*$, we obtain immediately:

$$\dot{\boldsymbol{\delta}}_\mathbf{f} \quad = \quad -\boldsymbol{\omega} \times \boldsymbol{\delta}_f - \mathbf{M}\mathbf{Q}\boldsymbol{v}. \tag{31}$$

Taking the time derivative of the storage function $\mathcal{L} = \frac{1}{2}|\boldsymbol{\delta}_\mathbf{f}|^2$ and substituting for (31) yields:

$$\dot{\mathcal{L}} = -\boldsymbol{\delta}_\mathbf{f}^\top \mathbf{M}\mathbf{Q}\boldsymbol{v}. \tag{32}$$

With the new image feature $\mathbf{f}$, we have considered three control laws.

3.6.1 GAS control law

If we choose for the control law

$$\boldsymbol{\upsilon} = k_{\mathbf{M}}\mathbf{M}\boldsymbol{\delta}_{\mathbf{f}}, \quad k_{\mathbf{M}} > 0, \tag{33}$$

we obtain using (32) $\dot{\mathcal{L}} = -k_{\mathbf{M}}\boldsymbol{\delta}_{\mathbf{f}}^{\top}\mathbf{M}(\mathbf{q})\mathbf{Q}\mathbf{M}(\mathbf{q})\boldsymbol{\delta}_{\mathbf{f}}$. Since $\mathbf{Q}$ is a positive definite matrix and $\mathbf{M}(\mathbf{q})$ is a symmetric and non singular matrix (see (30)), classical Lyapunov theory guarantees that $\boldsymbol{\delta}_{\mathbf{f}}$ converges exponentially to zero.

Note that convergence rates of the components of the error $\boldsymbol{\delta}_{\mathbf{f}}$ are given by the eigenvalues of $\mathbf{MQM}$. Let $\boldsymbol{\xi}$ denote the camera position with respect to the target, expressed in the camera frame. We have of course $\dot{\boldsymbol{\xi}} = -\boldsymbol{\omega} \times \boldsymbol{\xi} + \boldsymbol{\upsilon}$. Since $\mathbf{f}$ is chosen to be an approximated estimation of the target position with respect to the camera, we have $\mathbf{f} \simeq -\boldsymbol{\xi}$, and then $\dot{\mathbf{f}} \simeq -\boldsymbol{\omega} \times \mathbf{f} - \boldsymbol{\upsilon}$. Recalling (29), we deduce $\mathbf{MQ} \simeq \mathbf{I}_3$. Thus we have $\mathbf{MQM} \simeq \mathbf{Q}^{-1}$.

As can be seen on Fig. 8, convergence of components x and y is unacceptably slow. This is due to the fact that $\mathbf{M} \simeq \mathbf{Q}^{-1}$ is not well-conditioned. $\lambda_{\min}(\mathbf{Q})$ becomes $\lambda_{\max}(\mathbf{Q}^{-1})$ which is the third eigenvalue of matrix $\mathbf{Q}^{-1}$, and affects the z component. This situation is the opposite of the one exposed in Section 3.3 where convergence of the z component was unacceptably slow. In the present case, the z component is affected by $\lambda_{\max}(\mathbf{Q})$ and converges quickly with respect to the others.

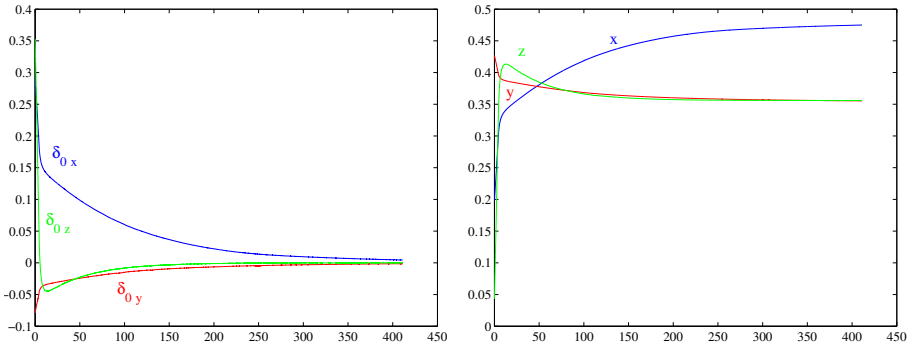

(a) (b)

Figure 8: GAS control design $\boldsymbol{\upsilon} = k_{\mathbf{M}}\mathbf{M}\boldsymbol{\delta}_{\mathbf{f}}$: time evolution of the image feature $\boldsymbol{\delta}_0 = \mathbf{R}\boldsymbol{\delta}_{\mathbf{f}}$ (a), and of the pose $\boldsymbol{\xi}_0$ (b).

Although this control law ensures global asymptotic stability, the task space and image space behaviour are not acceptable.

3.6.2 Proportional feedback

Since $\mathbf{f} \simeq -\boldsymbol{\xi}$ an intuitive idea is to choose

$$\boldsymbol{\upsilon} = k_{\mathbf{f}}\boldsymbol{\delta}_{\mathbf{f}}, \quad k_{\mathbf{f}} > 0. \tag{34}$$

Then recalling (32) we obtain for the derivative of the storage function: $\dot{\mathcal{L}} = -k_{\mathbf{f}} \boldsymbol{\delta}_{\mathbf{f}}^{\top} \mathbf{M}\mathbf{Q}\boldsymbol{\delta}_{\mathbf{f}}$.

Since $\mathbf{MQ} \simeq \mathbf{I}_3$, we have approximately the same convergence rate for the components of the error.

As expected the behaviour is very satisfactory in task space and in image space (Fig. 9.a and 9.b). The three components converge at equal rates, the transient behaviour is suitable, and the desired position is reached in reasonable number of iterations.

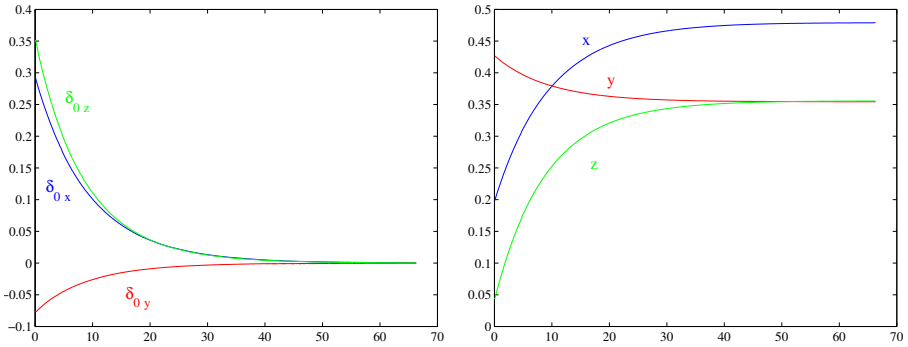

(a) (b)

Figure 9: Proportional control $\boldsymbol{\upsilon} = k_{\mathbf{f}} \boldsymbol{\delta}_{\mathbf{f}}$: time evolution of the image feature $\boldsymbol{\delta}_0 = \mathbf{R}\boldsymbol{\delta}_{\mathbf{f}}$ (a), and of the pose $\boldsymbol{\xi}_0$ (b).

However the limitation of this control scheme is that we cannot demonstrate the global asymptotic stability because we are not sure to have $\mathbf{MQ} > \mathbf{0}$ in all the task space.

3.6.3 Classical control law with approximate cancellation of interaction matrix

As already said in Section 3.4, the classical control law $\boldsymbol{\upsilon} = k_{\mathbf{Q}} \mathbf{Q}^{-1} \boldsymbol{\delta}$, $k_{\mathbf{Q}} > 0$ can not be used in practice, since $\mathbf{Q}$ depends on the 3D depths $|\mathbf{P}_i|$. In Section 3.4 we use the desired interaction matrix $\mathbf{Q}^*$, as usually in such situation.

Since $\mathbf{MQ} \simeq \mathbf{I}_3$, $\mathbf{M}$ provides an approximation of the interaction matrix $\mathbf{Q}^{-1}$, and an alternative choice is thus to use $\mathbf{M}$ instead of $\mathbf{Q}^*$ in the control law (18).

We obtain the following control law,

$$\boldsymbol{\upsilon} = k_{\mathbf{q}} \mathbf{M} \boldsymbol{\delta}, \; k_{\mathbf{q}} > 0. \tag{35}$$

Since $\mathbf{M}$ is not constant, better results than in Section 3.4 are expected. However, as can be seen on Fig.10, the behaviour in the task space is not really improved; once more, the transient in the depth component is not acceptable.

The proposed approximation $\mathbf{M} \simeq \mathbf{Q}^{-1}$, equally as the previous asymptotic compensations (Sections 3.4 and 3.5) are not sufficient to overcome the problem of sensitivity in the z-axis.

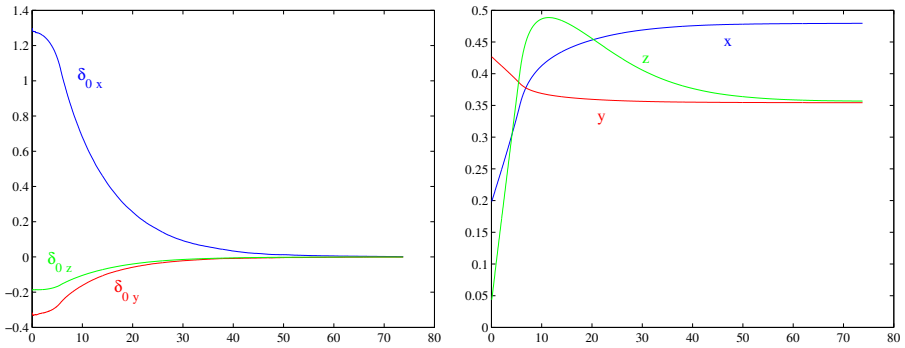

(a) (b)

Figure 10: Approximate cancellation of interaction matrix $\boldsymbol{\upsilon} = k_{\mathbf{q}}\mathbf{M}\boldsymbol{\delta}$: time evolution of the image feature $\boldsymbol{\delta}_0 = \mathbf{R}\boldsymbol{\delta}$ (a), and of the pose $\boldsymbol{\xi}_0$ (b).

3.7 GAS control law with modified rescaled image feature

In this subsection we attempt to define a new image feature and control law that combine the properties of good transient behaviour, good local exponential stability and global asymptotic stability. The approach taken is to define a new scaling function $G(|\mathbf{q}|)$ and scaled image feature

$$\mathbf{g} = G(|\mathbf{q}|)\mathbf{q}_0 \tag{36}$$

with

$$\dot{\mathbf{g}} = -\boldsymbol{\omega} \times \mathbf{g} - \mathbf{H}\mathbf{Q}\boldsymbol{\upsilon} \tag{37}$$

where $G(|\mathbf{q}|)$ can be chosen so that $\mathbf{H}$ induces good properties for asymptotic stability of the resulting control law. Similar developments to Section 3.6 for the derivation of $\mathbf{M}$ give the relationship between matrix $\mathbf{H}$ and function $G(|\mathbf{q}|)$:

$$\mathbf{H}(\mathbf{q}) = \frac{\partial G(|\mathbf{q}|)}{\partial |\mathbf{q}|}\mathbf{q}_0\mathbf{q}_0^\top + \frac{G(|\mathbf{q}|)}{|\mathbf{q}|}(\mathbf{I}_3 - \mathbf{q}_0\mathbf{q}_0^\top). \tag{38}$$

The error $\boldsymbol{\delta}_{\mathbf{g}}$ is defined as follows

$$\boldsymbol{\delta}_{\mathbf{g}} = \mathbf{g} - \mathbf{g}^* = G(|\mathbf{q}|)\mathbf{q}_0 - G(|\mathbf{q}^*|)\mathbf{q}_0^*.$$

Recalling (37) the dynamics of this error function is given by $\dot{\boldsymbol{\delta}}_{\mathbf{g}} = -\boldsymbol{\omega} \times \boldsymbol{\delta}_{\mathbf{g}} - \mathbf{H}\mathbf{Q}\boldsymbol{\upsilon}$, and we can note that $\boldsymbol{\delta}_{\mathbf{g}}$ ensures the passivity property, as expected from the choice of $\mathbf{g}$.

The natural idea to ensure GAS is to choose as control law $\boldsymbol{\upsilon} = k_{\mathbf{g}}\mathbf{H}\boldsymbol{\delta}_{\mathbf{g}}$, $k_{\mathbf{g}} > 0$, since we will obtain for the derivative of the storage function $\mathcal{L} = \frac{1}{2}|\boldsymbol{\delta}_{\mathbf{g}}|^2$: $\dot{\mathcal{L}} = -k_{\mathbf{g}}\boldsymbol{\delta}_{\mathbf{g}}^\top\mathbf{H}\mathbf{Q}\mathbf{H}\boldsymbol{\delta}_{\mathbf{g}}$.

Since $\mathbf{Q}$ is a positive definite matrix and $\mathbf{H}$ is a symmetric and non singular matrix (see (38)), classical Lyapunov theory guarantees that $\boldsymbol{\delta}_\mathbf{g}$ converges exponentially to zero. The convergence rates of $\boldsymbol{\delta}_\mathbf{g}$ will be given by the eigenvalues of $\mathbf{HQH}$, thus the idea is then to choose $\mathbf{H}$ such that $\mathbf{HQH}$ is well-conditioned and as near as $\mathbf{I}_3$ as possible. Since $\mathbf{M} \simeq \mathbf{Q}^{-1}$, an intuitive choice for $\mathbf{H}$ is $\mathbf{H} = \sqrt{\mathbf{M}}$, since in that case we will have $\mathbf{HQH} \simeq \mathbf{I}_3$.

In practice, the problem above has no solution because the constraints are too restrictive. Relaxing this constraint by introducing an additional parameter $\alpha(|\mathbf{q}|)$ such that $\mathbf{HQH} \simeq \alpha(|\mathbf{q}|)^2\mathbf{I}_3$ and $\alpha(|\mathbf{q}^*|) = 1$ enable us to determine a solution. The function $\alpha(|\mathbf{q}|)$ is derived as the solution of differential equation. Details are given in the appendix.

Choosing the control law

$$\boldsymbol{\upsilon} = k_\mathbf{g} \frac{\mathbf{H}(\mathbf{q})}{\alpha(|\mathbf{q}|)^2} \boldsymbol{\delta}_\mathbf{g}, \quad k_\mathbf{g} > 0, \tag{39}$$

the derivative of the storage function is given by

$$\dot{\mathcal{L}} = -k_\mathbf{g} \boldsymbol{\delta}_\mathbf{g}^\top \frac{\mathbf{H}(\mathbf{q})\mathbf{Q}\mathbf{H}(\mathbf{q})}{\alpha(|\mathbf{q}|)^2} \boldsymbol{\delta}_\mathbf{g} \tag{40}$$

and Lyapunov theory guarantees that $\boldsymbol{\delta}_\mathbf{g}$ converges exponentially to zero.

The convergence rates of $\boldsymbol{\delta}_\mathbf{g}$ are now given by the eigenvalues of $\frac{\mathbf{H}(\mathbf{q})\mathbf{Q}\mathbf{H}(\mathbf{q})}{\alpha(|\mathbf{q}|)^2}$, and the feature $\boldsymbol{\delta}_\mathbf{g}$ has been designed such that $\mathbf{H}(\mathbf{q})\mathbf{Q}\mathbf{H}(\mathbf{q}) \simeq \alpha(|\mathbf{q}|)^2\mathbf{I}_3$ and $\alpha(|\mathbf{q}^*|)^2 = 1$. This ensures good local exponential stability of $\boldsymbol{\delta}_\mathbf{g}$.

The new image feature $\mathbf{g} = G(|\mathbf{q}|)\mathbf{q}_0$, and the previous feature $\mathbf{f} = F(|\mathbf{q}|)\mathbf{q}_0$ are designed in the same manner: the direction of the feature is given by $\mathbf{q}_0$, and the norm is given by the scaling factor $G(|\mathbf{q}|)$ and $F(|\mathbf{q}|)$ respectively. $G(|\mathbf{q}|)$ provides a less aggressive scaling correction than $F(|\mathbf{q}|)$ as seen in Fig. 11. This improves the sensitivity of the image feature to pixel noise and improves robustness of the closed-loop system. A disadvantage of the new image feature $\mathbf{g}$ is that it is not as closely linked to the actual task space coordinates as the feature $\mathbf{f}$ (or the 2D perspective moments used in Section 2). Since $F(|\mathbf{q}|)$ is an approximation of the depth, the feature $\mathbf{f} = F(|\mathbf{q}|)\mathbf{q}_0$ is directly related to the 3D position. In case of the feature $\mathbf{g}$, using the scale factor $G(|\mathbf{q}|) = \alpha(|\mathbf{q}|)\sqrt{|\mathbf{q}|F(|\mathbf{q}|)}$, the relationship between image space and task space is non linear (see Fig. 11). This leads to some degradation of the global transient behaviour for certain initial conditions. However, this issue had limited effect on the observed performance of the closed-loop system in practice.

As expected, in addition to the global asymptotic stability, this control scheme ensures suitable image space convergence as can be seen on Fig. 12.a. Moreover a satisfactory 3D behaviour is obtained (see Fig. 12.b).

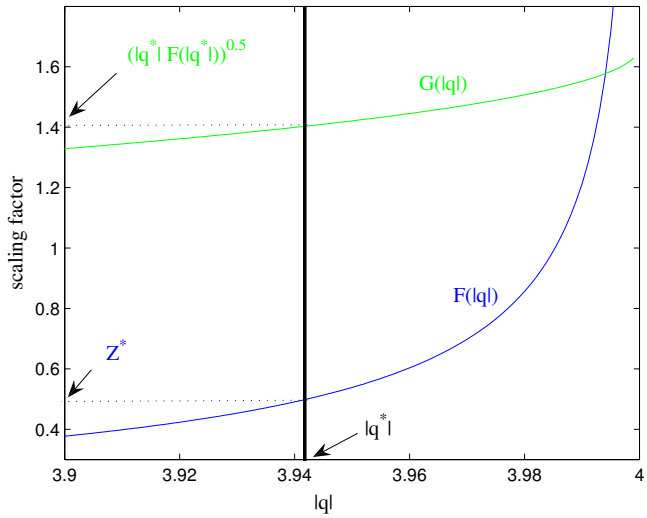

Figure 11: Plot of the scaling factors $F(|\mathbf{q}|) = \frac{R|\mathbf{q}|}{\sqrt{n^2-|\mathbf{q}|^2}}$ and $G(|\mathbf{q}|) = \alpha(|\mathbf{q}|)\sqrt{|\mathbf{q}|F(|\mathbf{q}|)}$ (with R=0.086, n=4), in the zone used for the experimental results. Note that $F(|\mathbf{q}^*|) = Z^*$ and $G(|\mathbf{q}^*|) = \sqrt{|\mathbf{q}^*|Z^*}$.

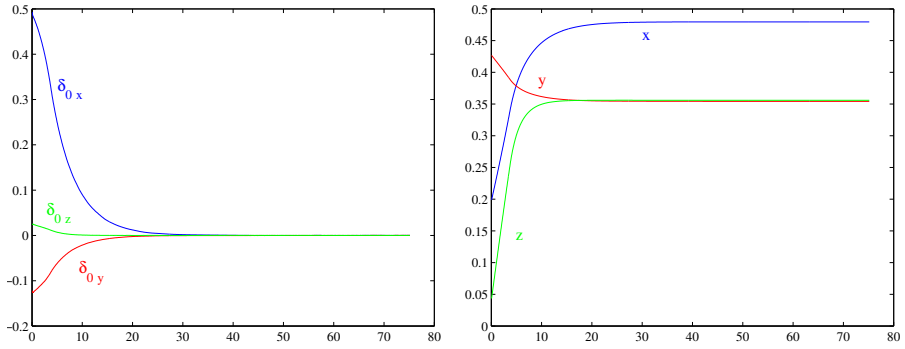

Figure 12: Rescaled image feature $\boldsymbol{\upsilon} = k_{\mathbf{g}}\frac{\mathbf{H}(\mathbf{q})}{\alpha(|\mathbf{q}|)^2}\boldsymbol{\delta}_{\mathbf{g}}$: time evolution of the image feature $\boldsymbol{\delta}_0 = \mathbf{R}\boldsymbol{\delta}_{\mathbf{g}}$ (a), and of the pose $\boldsymbol{\xi}_0$ (b).

4 Analysis

4.1 Properties of the control laws

A range of image based visual servoing schemes has been presented in Sections 2 and 3. Table 1 gives summary of the properties for each control scheme, in term of stability, transient behaviour, linearity, and passivity.

In practice, two of the most important properties are good transient conditioning (direct convergence of all elements of position in task space without any observed divergence or peaking transients), and balanced local exponential stability (equal asymptotic rate of convergence in all axis of the position in task space). Control laws *2* and *5* do not display balanced locally exponentially stability. The convergence rates of the three components are not equal, leading to unacceptable asymptotic closed-loop behaviour in practice. Control laws *3, 4* and *7* do not display suitable transient behaviour, leading to unacceptable closed-loop response in practice.

Three control schemes have good behaviour in practice: the perspective image moments (control scheme *1*), the rescaled proportional feedback (control scheme *6*), and the modified rescaled control (control scheme *8*).

A linear relationship between task space and image space is also very useful in practice. IBVS control laws ensure a desired trajectory in the feature space. If the correspondence between image feature and task space position is approximately linear then good transients in image space will correspond to good transient response in task space.

Two other properties of the closed-loop system are important. Global asymptotic stability (GAS) is ensured theoretically for several of the control laws using a Lyapunov function stability argument. A final property that is of interest is the decoupling of the closed-loop response in translation from variation in the attitude of the system. This property is referred to as passivity of the closed-loop response due to its link with earlier work [12] that exploits the structure of the spherical image surface to preserve natural passivity properties of rigid-body motion in the image space dynamics.

4.2 Comparison of the three best control laws

The classical perspective image moments controller (control law *1*) provides a linear correspondence between image space and task space as long as the relative rotation between image and target plane is small. The resulting closed-loop system response is expected to be satisfactory both in transient performance and asymptotic convergence and in both image and task space (kinematic experimental results can be found in [24]). However, as consequence of the limiting assumptions on the rotation, the system is not GAS nor passive. Moreover, it is expected that strong rotational motion will significantly disturb the performance of the system.

The rescaled proportional feedback using spherical image moments (control law *6*) has the same desirable image feature properties as control law *1*. In fact the rescaled visual feature $\mathbf{f} = F(|\mathbf{q}|)\mathbf{q}_0$ is very close to the 3D position, analogously to the visual features used

	Scheme	Control law	GAS	BLES	TC	ALR	P
1.	Perspective image moments (Section 2)	$\boldsymbol{v} = \lambda \mathbf{e}$	×	√	good	√	×
2.	Proportional control (Section 3.3)	$\boldsymbol{v} = k\boldsymbol{\delta}$	√	×	bad	×	√
3.	Linearization at the set point (Section 3.4)	$\boldsymbol{v} = k_* \mathbf{Q}^{*-1}\boldsymbol{\delta}$	×	√	poor	×	√
4.	Partitioned control (Section 3.5)	$\boldsymbol{v} = k_{\mathbf{A}} \mathbf{A} (\mathbf{q}_0^*)^\top \boldsymbol{\delta}_{\mathbf{A}}$	√	√	poor	×	√
5.	Rescaled stable control (Section 3.6.1)	$\boldsymbol{v} = k_{\mathbf{M}} \mathbf{M}\boldsymbol{\delta}_{\mathbf{f}}$	√	×	bad	×	√
6.	Rescaled proportional feedback (Section 3.6.2)	$\boldsymbol{v} = k_{\mathbf{f}} \boldsymbol{\delta}_{\mathbf{f}}$	×	√	good	√	√
7.	Approximate interaction matrix (Section 3.6.3)	$\boldsymbol{v} = k_{\mathbf{q}} \mathbf{M}\boldsymbol{\delta}$	×	√	poor	×	√
8.	Modified rescaled control (Section 3.7)	$\boldsymbol{v} = k_{\mathbf{g}} \frac{\mathbf{H}(\mathbf{q})}{\alpha(\lvert\mathbf{q}\rvert)^2} \boldsymbol{\delta}_{\mathbf{g}}$	√	√	good	×	√

Table 1: Properties of different control schemes considered in this paper.
Definitions of the acronyms used are as follows:

GAS : globally asymptotically stable,
BLES : balanced locally exponentially stable,
TC : transient conditioning,
ALR : approximately linear relationship between task space and image space,
P : passivity.

in control law *1*. The control laws are a simple proportional feedback in the two cases. The advantage of the spherical image moments is that they ensure the passivity property, and should be more robust to aggressive manoeuvres of an aerial vehicle as well as leading more naturally to a full dynamic image based visual servo control design. A potential problem, however, is the requirement to estimate the camera attitude in order to reconstruct the image based error term. There is no formal proof of GAS for control law *6*, however, due to the natural structure of the image feature the authors expect that the domain of stability for this control law will be sufficiently large that unstable behaviour will not be encountered in practice.

The last suitable control law (*8*) is based on a modified rescaled visual feature, in order to ensure GAS. This control law provides the guarantee of GAS that is missing in control law *6*. Its only drawback is that the visual feature is no longer linearly related to the 3D position and this may lead to slightly degraded transient response in task space.

All three of the control schemes *1, 6* and *8* are potentially good control algorithms in practice. Each algorithm has certain advantages and certain drawbacks. The exact approach taken for a given application should depend on the particular requirements of that application.

5 Experimental results

In this section we provide experimental verification of the performance of the three preferred image based control schemes presented earlier in the paper on an aerial robotic vehicle. The control algorithms considered are classical control using the well-known perspective zero and first order image moments (Section 2), proportional feedback using the spherical image moments rescaled with F (Section 3.6.2), and GAS control law using the spherical image moments rescaled with G (Section 3.7)). The experiments were undertaken on a quadrotor aerial vehicle. The task considered is to stabilise the vehicle with respect to a specified target.

5.1 Experimental conditions

5.1.1 Prototype description

Figure 13: A quadrotor.

The unmanned aerial vehicle used for the experimentations is a quadrotor (Fig.13), that is an omnidirectional VTOL vehicle ideally suited for stationary and quasi-stationary flight conditions. It consists of four fixed pitch propellers linked to an electrical motor at each extremity of a cross frame (Fig. 13). The vehicle is equipped with an avionics stack including an Inertial Measurement Unit (IMU) supplying the vehicle attitude and a controller board [11, 10]. A wireless link allows the transmission of the attitude command between the quadrotor and a ground station (Pentium 4). A camera situated below the quadrotor (Fig. 14.a) is embedded and observes a target on the ground, consisting of four black marks on the vertices of a planar rectangle (30×40 cm) (Fig. 14.b). A wireless analogue link transmits camera images to the ground station. A 3D estimation of the vehicle position with respect to the target is obtained by fusing the data of the embedded IMU and the visual data in a particle filter [2]. This estimate is used to provide an estimate of ground

truth for the 3D behaviour of the vehicle and to provide an estimate of the linear velocity of the vehicle that is used by the high-gain controller of the airframe dynamics. In this paper, only 2D visual information is used in the outer IBVS control loop for position regulation. All the visual servo controls tested are implemented on the ground station.

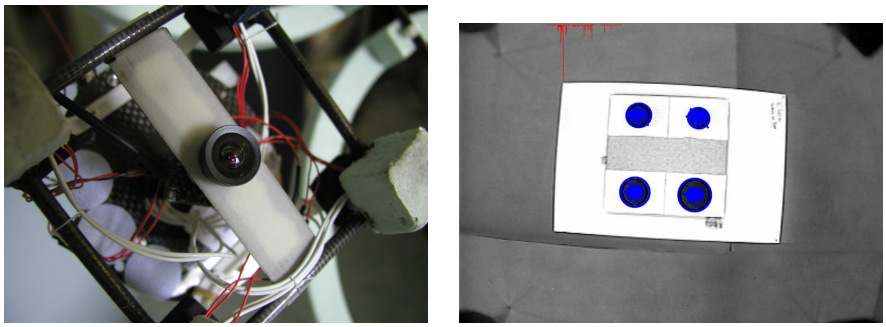

(a) (b)

Figure 14: The camera (a), and the target view from the camera (b).

5.1.2 Experimental protocol

In order to compare the proposed different kinematic visual servo controls, the initial conditions of the experiments were chosen identically. For each experiment, the quadrotor was servo controlled to a specific initial position using a standard state-space controller deriving information from the task space position estimate. When the vehicle was stabilised at this position, the visual control was initiated and the 3D position, obtained from a particle filter, was recorded. This protocol ensures that the flight conditions are the same and allows the comparison between the different controllers. The velocity demand was also saturated at 20 cm/s to ensure the vehicle remains in quasi-stationary flight regime [12].

The asymptotic value for the matrix $\mathbf{Q}$ is

$$\mathbf{Q}^* = \mathrm{diag}(2.35, 2.36, 0.057) \tag{41}$$

and we have $\mathbf{b} \cong (0, 0, 3.96)$. These values have been computed when the vehicle is situated at the desired position: approximatively above the center of the target at 1.4 m height of the ground.

In the following subsections, the three preferred kinematic image based control schemes for the translational motion of the quadrotor are considered. For each experiment, the 3D position of the camera in the task space reference frame is depicted, along with the velocity output of the visual servo control law. The evolution of the visual error considered is also depicted, as well as the trajectory of the four black marks in the image plane.

5.2 Perspective image moments

The first experiment is using the perspective image moments proposed in [24], with the approximation of small rotations. The control law used is thus very simple: $\boldsymbol{v} = \lambda \mathbf{e}$ (see Section 2). The practical results are very satisfactory (see Figure 15). Moreover, the control law is a simple proportional control, and, as the visual error design needs only visual data, it is very easily implemented.

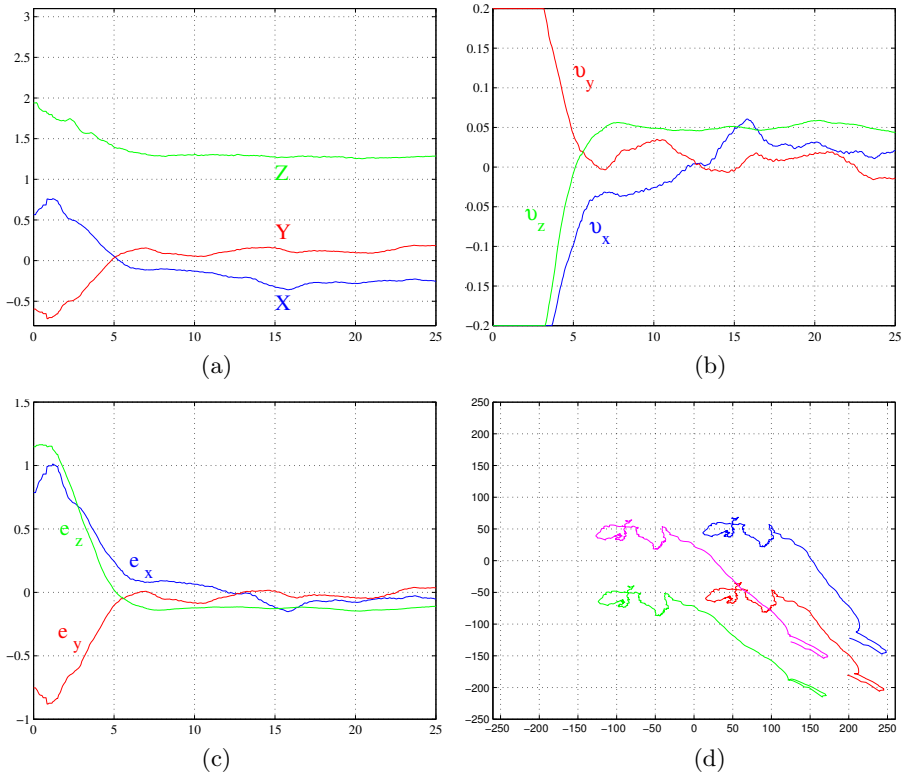

Figure 15: $\boldsymbol{v} = 0.4\mathbf{e}$: time evolution (in seconds) of the real position in the task space (in meters) (a) with the velocity output of the visual servo control $\boldsymbol{v}$ (in meters per seconds) (b). The evolution of the visual error is plotted on (c), and the trajectory of the four black marks in the image plane are plotted on (d).

5.3 Spherical image moments

5.3.1 Proportional feedback

The proportional control law $\boldsymbol{\upsilon} = k_{\mathbf{f}}\boldsymbol{\delta}_{\mathbf{f}},\ k_{\mathbf{f}} > 0$, using the rescaled feature $\mathbf{f} = F(|\mathbf{q}|)\mathbf{q}_0$ gave very satisfactory results with the six degrees of freedom robot (see Section 3.6.2).

As expected, the behaviour of the quadrotor is very good. Transient is acceptable and the three components converge at equal rates equally in image space as in task space (see Fig. 16).

As for the previous control law, its advantage is also that it is easily implemented, since the control law is a direct function of the visual error $\boldsymbol{\delta}_{\mathbf{f}}$. Since this control law has the additional passivity property, it is expected to be well-adapted for wide range of aerial vehicles and experimental conditions.

However, similar to the perspective moments control design, the global asymptotic stability has not been demonstrated.

5.3.2 GAS control law

The last experiment used the control law $\boldsymbol{\upsilon} = k_{\mathbf{g}}\frac{\mathbf{H}(\mathbf{q})}{\alpha(|\mathbf{q}|)^2}\boldsymbol{\delta}_{\mathbf{g}},\ k_{\mathbf{g}} > 0$, with the new rescaled feature $\mathbf{g} = G(|\mathbf{q}|)\mathbf{q}_0$ (see Section 3.7).

As can be seen on Fig. 17, this control scheme leads to equal convergence rates of the visual error components, and equal convergence rates in the task space. The transient behaviour is acceptable.

This control law ensures good behaviour as well as the theoretical important properties of GAS and passivity. However the linear link between task space and image space is destroyed, and this could lead to undesirable transient behaviour in some situations.

5.4 Noise sensitivity

At first glance, the results (see Fig. 15, Fig. 16, and Fig. 17), for the three control schemes are very similar.

A potential problem with the control laws *6* and *8* is that the rotation matrix $\mathbf{R}$ between the camera frame and the inertial frame has to be estimated. However this estimation does not seem to introduce noise, delay or any significant perturbations in practice (compare Fig. 15 with Fig. 16 and Fig. 17).

To better understand the noise sensitivity of each control scheme, we have computed the root mean-square error (RMSE) of the velocity demand over the period between 10 and 25 seconds, during which period all three closed-loop systems are stabilised in a neighbourhood of the set point. Note that to get rid of the effect of the gains, we consider the velocity output without the gains λ, $k_{\mathbf{f}}$ and $k_{\mathbf{g}}$.

We compute

$$\sigma_{\boldsymbol{\upsilon}} = \sqrt{\sigma_{\upsilon_X}^2 + \sigma_{\upsilon_Y}^2 + \sigma_{\upsilon_Z}^2}$$

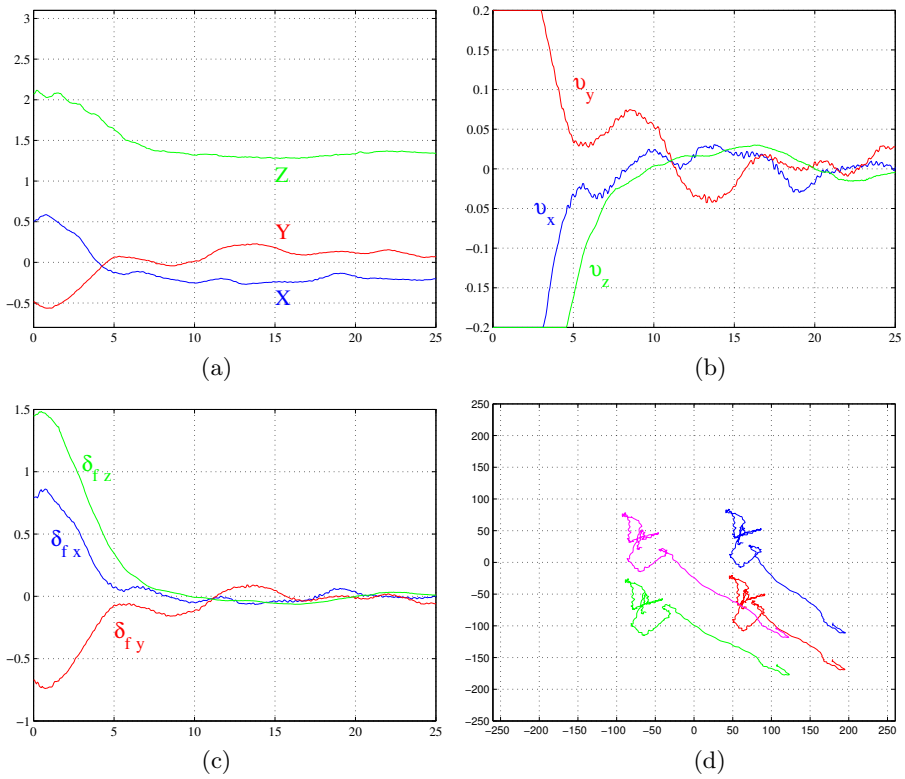

Figure 16: $\boldsymbol{\upsilon} = 0.47\boldsymbol{\delta_f}$: time evolution (in seconds) of the real position in the task space (in meters) (a) with the velocity output of the visual servo control $\boldsymbol{\upsilon}$ (in meters per seconds) (b). The evolution of the visual error is plotted on (c), and the trajectory of the four black marks in the image plane are plotted on (d).

along with $\sigma_{\upsilon_K} = \sqrt{\sum_i (\upsilon_{K_i} - \bar{\upsilon}_K)^2}$, for $K \in [X, Y, Z]$ and where $\bar{\upsilon}_K$ is the average of υ_K between 10 and 25 seconds.

As can be seen on Table 2, the noise measured at the output of all control laws are very similar. The three control laws have very similar behaviour with respect to the noise.

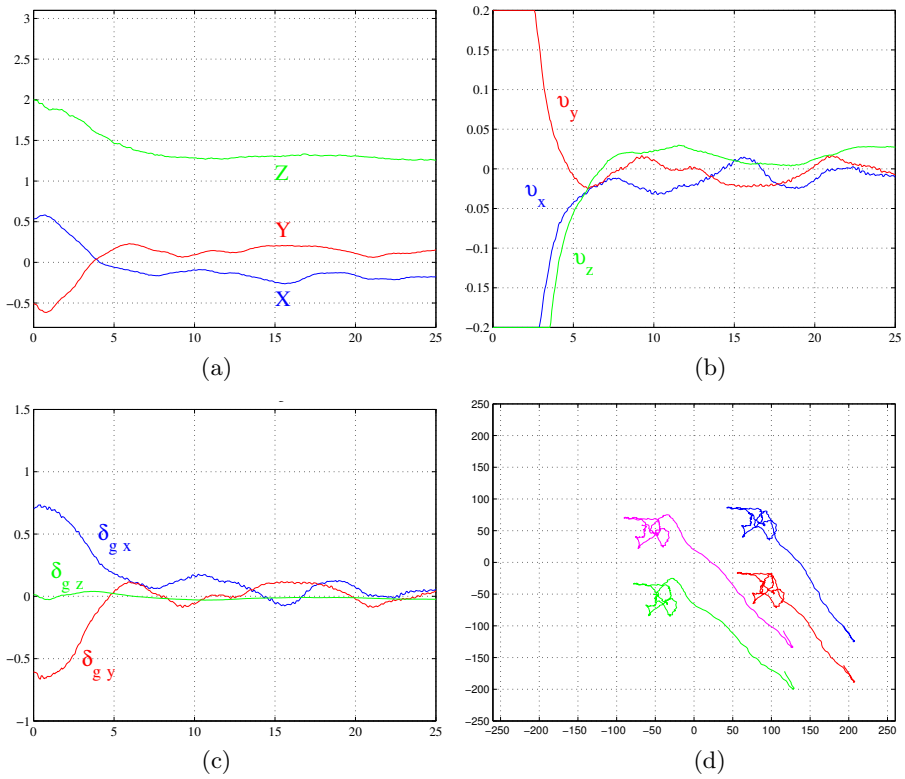

Figure 17: $\boldsymbol{\upsilon} = 0.3\frac{\mathbf{H(q)}}{\alpha(|\mathbf{q}|)^2}\boldsymbol{\delta}_\mathbf{g}$: time evolution (in seconds) of the real position in the task space (in meters) (a) with the velocity output of the visual servo control $\boldsymbol{\upsilon}$ (in meters per seconds) (b). The evolution of the visual error is plotted on (c), and the trajectory of the four black marks in the image plane are plotted on (d).

	$\sigma_{\boldsymbol{\upsilon}}$	σ_{υ_X}	σ_{υ_Y}	σ_{υ_Z}
$\boldsymbol{\upsilon} = \mathbf{e}$	0.95	0.79	0.51	0.15
$\boldsymbol{\upsilon} = \boldsymbol{\delta}_\mathbf{f}$	1.02	0.51	0.74	0.49
$\boldsymbol{\upsilon} = \frac{\mathbf{H}}{\alpha^2}\boldsymbol{\delta}_\mathbf{g}$	1.01	0.65	0.61	0.47

Table 2: Root mean-square error (RMSE) of the velocities for each control law

6 Conclusion

This paper has investigated a suite of image based kinematic visual servo control schemes to control a quadrotor. Using the well-known perspective image moments to design a classical IBVS translational control law leads to good system behaviour in the experimental studies undertaken. However this control scheme does not ensure global asymptotic stability or passivity of the closed-loop system, both properties that the authors believe will be important for the development of fully dynamic IBVS control schemes in the future. First order spherical image moments along with an inertial goal vector allow us to design translational control laws independent from the rotation motion. Global asymptotic stability is obtained by using these visual features and a simple proportional feedback, but the behaviour on the z-axis is not acceptable. A range of control laws is proposed in order to improve the behaviour of the system. The most promising approach investigated involves rescaling the spherical image moments to obtain an image feature that minimises the sensitivity in the depth axis. Experimental results using a 6 degrees of freedom holonomic robot are reported for each control laws, that show the fundamental properties of the closed-loop system for each approach.

The perspective image moments control design, as well as two of the control laws using spherical image moments were implemented on the quadrotor. In practice all three control algorithms lead to acceptable behaviour of the system.

Appendix

This appendix describes the derivation of a rescaled image feature $\mathbf{g} = G(|\mathbf{q}|)\mathbf{q}_0$ that will satisfy the following two properties.

1. Passivity: this will be ensured if $\dot{\mathbf{g}} = -\boldsymbol{\omega} \times \mathbf{g} - \mathbf{H}\mathbf{Q}\boldsymbol{\upsilon}$ where $\mathbf{H}$ is a matrix related to the scaling function G by (cf. (38))

$$\mathbf{H}(\mathbf{q}) = \frac{\partial G(|\mathbf{q}|)}{\partial |\mathbf{q}|}\mathbf{q}_0\mathbf{q}_0^\top + \frac{G(|\mathbf{q}|)}{|\mathbf{q}|}\big(\mathbf{I}_3 - \mathbf{q}_0\mathbf{q}_0^\top\big). \tag{42}$$

2. GAS: this is obtained if $\mathbf{H}$ has the following form: $\mathbf{H}(|\mathbf{q}|) = \alpha(|\mathbf{q}|)\sqrt{\mathbf{M}}$.

Recalling (30) and imposing the structure of constraint 2) one obtains:

$$\begin{aligned}\mathbf{H}(\mathbf{q}) \quad = \quad & \alpha(|\mathbf{q}|)\sqrt{\frac{\partial F(|\mathbf{q}|)}{\partial |\mathbf{q}|}}\mathbf{q}_0\mathbf{q}_0^\top \\ & + \alpha(|\mathbf{q}|)\sqrt{\frac{F(|\mathbf{q}|)}{|\mathbf{q}|}}\big(\mathbf{I}_3 - \mathbf{q}_0\mathbf{q}_0^\top\big).\end{aligned} \tag{43}$$

By matching the terms of (42) and (43), one obtains:

$$G(|\mathbf{q}|) = \alpha(|\mathbf{q}|)\sqrt{|\mathbf{q}|F(|\mathbf{q}|)}, \tag{44}$$

$$\frac{\partial G(|\mathbf{q}|)}{\partial |\mathbf{q}|} = \alpha(|\mathbf{q}|)\sqrt{\frac{\partial F(|\mathbf{q}|)}{\partial |\mathbf{q}|}}. \tag{45}$$

Then deriving (44) and substituting in (45) gives

$$\alpha' = \frac{\alpha(|\mathbf{q}|)}{\sqrt{|\mathbf{q}|F(|\mathbf{q}|)}}\Big(\sqrt{F'} - \frac{F(|\mathbf{q}|) + |\mathbf{q}|F'}{2\sqrt{|\mathbf{q}|F(|\mathbf{q}|)}}\Big) \tag{46}$$

where $\alpha' = \frac{\partial \alpha(|\mathbf{q}|)}{\partial |\mathbf{q}|}$.

Using the definition of F (Eq. (27)), deriving it and replacing in (46), we obtain the ordinary differential equation

$$\alpha' = \alpha(|\mathbf{q}|)\Big(\frac{2n\sqrt{D} - 2n^2 + |\mathbf{q}|^2}{2|\mathbf{q}|D}\Big), \tag{47}$$

where $D = n^2 - |\mathbf{q}|^2$.

The solution of this equation is given by

$$\alpha(|\mathbf{q}|) = C(n, |\mathbf{q}^*|)\frac{D^{\frac{1}{4}}}{|\mathbf{q}|}\sqrt{\frac{n - \sqrt{D}}{n + \sqrt{D}}} \tag{48}$$

where $C(n, |\mathbf{q}^*|)$ is chosen such that $\alpha(|\mathbf{q}^*|) = 1$.

Finally, substituting α in (44) and using the expression of F (Eq. (27)), the scale factor $G(|\mathbf{q}|)$ is defined by

$$G(|\mathbf{q}|) = C(n, |\mathbf{q}^*|)\sqrt{R}\sqrt{\frac{n - \sqrt{D}}{n + \sqrt{D}}}. \tag{49}$$

Acknowledgements

This work was supported by the French National Center for Scientific Research (CNRS) under the project ROBEA-Robvolint National Program in Robotics (http://www.laas.fr/robea/) and the International Programs for Scientific Cooperation (PICS) between France and Australia on visual servo-control of unmanned aerial vehicles.

References

[1] R. L. Andersson. *A robot ping-pong player: experiment in real-time intelligent control*. MIT Press, Cambridge, MA, USA, 1988.

[2] S. Arulampalam, S. Maskell, N. J. Gordon, and T. Clapp. A tutorial on particle filters for on-line non-linear/non-gaussian bayesian tracking. *IEEE Transactions of Signal Processing*, 50(2):174–188, February 2002.

[3] O. Bourquardez, R. Mahony, T. Hamel, and F. Chaumette. Stability and performance of image based visual servo control using first order spherical image moments. In *IEEE/RSJ Int. Conf. on Intelligent Robots and Systems, IROS'06*, pages 4304–4309, Beijing, China, October 2006.

[4] F. Chaumette. Potential problems of stability and convergence in image-based and position-based visual servoing. In D. Kriegman, G . Hager, and A.S. Morse, editors, *The Confluence of Vision and Control*, pages 66–78. LNCIS Series, No 237, Springer-Verlag, 1998.

[5] F. Chaumette. Image moments: a general and useful set of features for visual servoing. *IEEE Trans. on Robotics*, 20(4):713–723, August 2004.

[6] P. Corke and S. A. Hutchinson. A new partitioned approach to image-based visual servo control. *IEEE Trans. Robot. Autom.*, 17(4):507–515, August 2001.

[7] B. Espiau, F. Chaumette, and P. Rives. A new approach to visual servoing in robotics. *IEEE Trans. on Robotics and Automation*, 8(3):313–326, June 1992.

[8] J. Feddema, C. S. G. Lee, and O. R. Mitchell. Weighted selection of image features for resolved rate visual feedback control. *IEEE Trans. on Robotics and Automation*, 7(1):31–47, February 1991.

[9] E. Frazzoli, M. A. Dahleh, and E. Feron. Real-time motion planning for agile autonomous vehicles. *Journal of Guidance Control and Dynamics*, 25(1):116–129, 2002.

[10] N. Guenard, T. Hamel, and L. Eck. Control law for the tele operation of an unmanned aerial vehicle known as an x4-flyer. In *IEEE/RSJ Int. Conf. on Intelligent Robots and Systems, IROS'06*, Beijing, China, October 2006.

[11] N. Guenard, T. Hamel, and V. Moreau. Dynamic modeling and intuitive control strategy for an x4-flyer. In *International Conference on Control and Automation*, Budapest, Hongrie, June 2005.

[12] N. Guenard, T. Hamel, V. Moreau, and R. Mahony. Design of a controller allowed the intuitive control of an x4-flyer. In *International IFAC Symposium on Robot Control*, University of Bologna (Italy), September 2006.

[13] T. Hamel and R. Mahony. Visual servoing of an under-actuated dynamic rigid-body system: an image based approach. *IEEE Trans. on Robotics and Automation*, 18(2):187–198, April 2002.

[14] T. Hamel and R. Mahony. Image based visual servo-control for a class of aerial robotic systems. *To appear in Automatica*, 2007.

[15] S. Hutchinson, G. Hager, and P. Corke. A tutorial on visual servo control. *IEEE Trans. on Robotics and Automation*, 12(5):651–670, 1996.

[16] M. Lei and B. K. Ghosh. Visually guided robotic motion tracking. In *Thirtieth Annual Conference on Communication, Control and Computing*, pages 712–721, 1992.

[17] R. Mahony, P. Corke, and F. Chaumette. Choice of image features for depth-axis control in image-based visual servo control. In *IEEE/RSJ Int. Conf. on Intelligent Robots and Systems, IROS'02*, volume 1, pages 390–395, Lausanne, Switzerland, October 2002.

[18] R. Mahony and T. Hamel. Robust trajectory tracking for a scale model autonomous helicopter. *International Journal of Non-linear and Robust Control*, 14:1035–1059, 2004.

[19] R. Mahony, T. Hamel, and F. Chaumette. A decoupled image space approach to visual servoing for a robotic manipulator. In *IEEE Int. Conf. on Robotics and Automation, ICRA'02*, Washington DC, Virginia, USA, 2002.

[20] E. Malis, F. Chaumette, and S. Boudet. 2 1/2 d visual servoing. *IEEE Transactions on Robotics and Automation*, 15(2):238–250, April 1999.

[21] R. Pissard-Gibollet and P. Rives. Applying visual servoing techniques to control of a mobile hand-eye system. In *IEEE Int. Conf. on Robotics and Automation, ICRA'95*, pages 166–171, Nagasaki, Japan, 1995.

[22] C. Samson, M. LeBorgne, and B. Espiau. Robot control: the task function approach. In *Oxford Engineering Science Series*, volume 22. Clarendon Press, Oxford, UK, 1991.

[23] A. Sanderson, L. Weiss, and C. Neuman. Dynamic sensor based control of robots with visual feedback. *IEEE Transactions on Robotics and Automation*, 3:404–417, 1987.

[24] O. Tahri and F. Chaumette. Point-based and region-based image moments for visual servoing of planar objects. *IEEE Transactions on Robotics*, 21(6):1116–1127, December 2005.

[25] B. Yoshimi and P. K. Allen. Active, uncalibrated visual servoing. In *IEEE Int. Conf. on Robotics and Automation, ICRA'94*, pages 156–161, San Diago, CA, USA, 1994.

Contents